Thermal stability and high-temperature behavior of the natural borate colemanite: an aggregate in radiation-shielding concretes.

Paolo Lotti[a]*, Davide Comboni[a], Lara Gigli[b], Lucia Carlucci[c], Eros Mossini[d], Elena Macerata[d], Mario Mariani[d], G. Diego Gatta[a,e]

[a] Dipartimento di Scienze della Terra, Università degli Studi di Milano, Via Botticelli 23, 20133 Milano, Italy.

[b] Elettra Sincrotrone Trieste S.c.P.A., Strada Statale 14 km 163.5, 34149 Basovizza, Trieste, Italy

[c] Dipartimento di Chimica, Università degli Studi di Milano, Via Golgi 19, 20133 Milano, Italy

[d] Dipartimento di Energia, Politecnico di Milano, Via Lambruschini 4, 20156 Milano, Italy.

[e] CNR – Istituto di Cristallografia, Sede di Bari, Via Amendola 122/o, 70126 Bari, Italy.

* Corresponding author

Email: paolo.lotti@unimi.it; Phone: +390250315598; Fax: +390250315597

Co-authors e-mails:

davide.comboni@unimi.it; lara.gigli@elettra.eu; lucia.carlucci@unimi.it; eros.mossini@polimi.it; elena.macerata@polimi.it; mario.mariani@polimi.it; diego.gatta@unimi.it

Declarations of interest: none

Abstract

Colemanite is a natural borate that can be used as an aggregate in neutron-radiation shielding concretes. In this study, we report its thermal behavior, up to 500°C, by describing: 1) its dehydration mechanisms and 2) its thermo-elastic parameters. The thermal expansion of colemanite is significantly anisotropic. The refined volume thermal expansion coefficient at ambient conditions is: $\alpha_{V0} = 4.50(10)\cdot10^{-5}$ K^{-1}. The loss of structural H_2O occurs at least from ~ 240 °C and at $T > 325$ °C, an irreversible amorphization occurs, followed by a complete dehydration. The potential implications on the use of colemanite as concrete-aggregate are discussed.

Keywords

Colemanite, boron, neutron radiation shielding concretes, high temperature, dehydration, amorphization, thermal expansion coefficient, synchrotron X-ray diffraction

1. Introduction

The need to protect workers and public exposed to radiation emitted, for example, by nuclear reactors for energy production or by neutron facilities for scientific research or medical applications requires the development and the production of suitable materials able to shield from harmful radiations. In this light, ^{10}B (which accounts for approximately the 20% of natural boron [1]) emerges as an interesting isotope for its elevated ability to absorb thermal neutrons due to its high cross section for $^{10}B(n,\alpha)^{7}Li$ reaction (3840 barns [2,3]). Consequently, neutrons reaction with ^{10}B suppresses escaping radiations and generates alpha particles (easily absorbable by few μm of material) and ^{7}Li, a stable isotope. It follows that boron compounds are target materials to be added as aggregates for the production of radiation-shielding concretes. Synthetic B_4C, for example, can be successfully used for this scope [4], but due to its high costs it is often replaced by cheaper natural borates [5]. Among them, colemanite, ideal formula $CaB_3O_4(OH)_3 \cdot H_2O$, is one of the major candidates, due to its large availability in nature and the resulting abundance of waste colemanite ore at the mining site, which recycling may result in an economic profit [6-8]. Colemanite is also largely utilized as a raw material for the production of boric acid [9]. For these reasons, the use of colemanite as an aggregate has been the subject of a series of investigations [10-14]. In the nuclear field, colemanite has been widely applied for the production of radiation-shielding concretes prototypes [5,15], which showed that its addition is efficient in reducing the transmission of radiation [5,10,12] and lowering the concrete activation for radiation emission in the low and medium term [11,15,16]. In fact, concrete containing colemanite or boron ores, in association with high-density aggregates, proved to possess low radioactive permeability and effectively prevent both neutrons and gamma radiation transmission [17-21]. These materials have been successfully employed not only as heavyweight concrete biological shield of nuclear reactors and research laboratories, but also of neutron therapy centers, such as radiation oncology and radiology departments [17].. Furthermore, the high radiation shielding property has been successfully applied to improve shielding from Am-Be sources, since they emit neutrons along with gamma radiations. The use of colemanite concrete proved to be an easier and more effective solution than distributing gamma shields (e.g. lead blocks) within neutron absorbing materials, such as paraffin [22-23]. In presence of high-energy gamma- and X-ray sources, the lower atomic number of elements constituting colemanite concrete represents a further advantage with respect to lead shields, in particular in the pair production and Compton scattering regions [17,24]. Moreover, with a view to ensure safe shipment of nuclear material, boron enriched cementitious containers have been proficiently proposed. In this perspective, the optimization of the neutron shielding effect requires a homogeneous distribution of boron within the cement matrix [25].

For its large availability and low costs, colemanite has also been investigated to be added in ordinary cements and mortars, lightweight concretes and bricks, and geopolymers [7,8,26-32]. By way of example, colemanite could be added to pumice lightweight concrete to improve its radiation shielding, thus extending the applicability of this low density and low cost, high thermal insulation and high durability material to the nuclear field [32]. These applications drove

the interest in studying the effects induced by the addition of colemanite on the physico-chemical properties of cements and concretes, from which it emerged that the major drawbacks are a delay in the cement setting and a lowering of the concrete compressive strength [14,17,26-29,32-34], even though they resulted to be less pronounced than those induced by two other common natural borates as ulexite and borax [34].

It is of the utmost importance to investigate the intrinsic properties at non-ambient conditions of the individual compounds making the cement and the aggregates, in order to understand and forecast the behavior of the concretes at the same conditions. In the case of a hydrous mineral like colemanite, for example, it is necessary to determine its high-temperature phase stability field, its thermal-elastic behavior (*i.e.*, bulk volume expansion and axial anisotropic scheme), how and when the temperature-induced release of structural H_2O occurs (taking into account that colemanite contains molecular H_2O and hydroxyl groups). Surprisingly, despite the interest driven by the applications of colemanite, only a few experiments have been focused to study its intrinsic thermal behavior [35-38]. The effect of mechanical treatment on colemanite thermal properties was studied, taking into consideration thermal stability and other thermodynamic parameters related to phase transition, such as structural relaxation and crystallization [39]. The modification of some colemanite physical properties, such as porosity, density and surface area, has been investigated as a function of temperature, up to 600 °C [30]. To the best of our knowledge, neither a structure refinement based on *in situ* high-*T* data, nor the *T*-induced evolution of the bulk volume and unit-cell parameters of colemanite has so far been reported and, therefore, its thermal behavior is not completely known.

In this light, the scope of this study is to provide, by means of *in situ* differential scanning calorimetry, thermogravimetric and synchrotron X-ray diffraction analyses, a clearer picture of the behavior of colemanite at high temperature by: 1) providing a thorough characterization of the dehydration process and of its influence on the structural stability and 2) quantifying the volume thermal expansion coefficient at ambient conditions and at varying temperature. This study is part of a long-term project devoted to the characterization of the behavior of B-containing compounds at non-ambient conditions [40-46], which included: 1) the study of the high-pressure behavior of colemanite, reporting a *P*-induced reconstructive phase transition, characterized by the increased coordination of a fraction of B atoms from triangular to tetrahedral [45], and 2) the study of the low-*T* behavior of colemanite, with the transition to its ferroelectric polymorph [46].

2. Crystal structure of colemanite

At ambient conditions, colemanite is monoclinic, space group $P2_1/a$, unit-cell parameters: $a \sim 8.74$, $b \sim 11.26$, $c \sim 6.10$ Å and $\beta \sim 110.12°$. Its crystal structure has been first solved by Christ et al. [47] and later refined by Christ et al. [48] and Clark et al. [49]. It is characterized by infinite chains of B-coordination polyhedra running along the **a** crystallographic axis (Figure 1). These chains are built by the repetition of the same corner-sharing building unit, made by one B atom in triangular coordination with oxygens, and two B atoms in tetrahedral coordination with both

oxygens and hydroxyl groups. The borate chains are linked along the **c** crystallographic direction by chains of corner-sharing Ca-coordination polyhedra (coordination number: 8, Figure 1), building up heteropolyhedral layers perpendicular to the **b** axis. Along that direction, the layers are interconnected by few Ca-O(H)-B bonds and an extensive network of H-bonds made by both the hydroxyl groups and the H_2O molecules [46], resulting in weaker connections along the **b** axis that are responsible for the perfect (010) cleavage plane observed in colemanite crystals. On cooling, at temperatures between 0 and -12°C, depending on the amount of chemical impurities [50], colemanite undergoes a phase transition toward a ferroelectric polymorph, still monoclinic, but with space group $P2_1$ and a slightly displaced atomic arrangement [46,51].

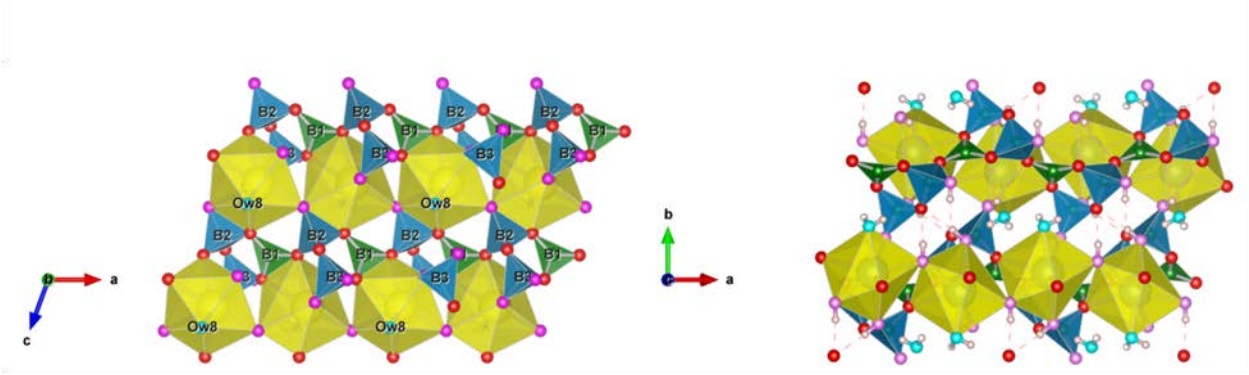

Figure 1. (*Left*) The crystal structure of colemanite viewed down the **b** crystallographic axis, showing the heteropolyhedral layers made by alternating borate and Ca-polyhedra chains. Every borate chain is made by the repetition of three-membered rings, formed by one boron site in triangular coordination and two boron sites in tetrahedral coordination. (*Right*). The colemanite structure viewed down the **c** axis: the heteropolyhedral layers are weakly interconnected by few Ca-O(H)-B bonds and by a network of H-bonds. These pictures have been created using the software VESTA [61].

3. Materials and experimental methods

The same natural sample of massive and transparent colemanite, already investigated and described by [45,46], has been used for this study. The sample, provided by the Museum of Mineralogy of the University of Padua (Italy), comes from the borate deposits of the Bigadiç Mine (Balikesir Province, Marmara Region, Turkey [52]). In order to perform the analyses described in the following section, the massive sample was ground in an agate mortar into a homogeneous powder.

The chemical analysis has been performed by means of a multi-methodological approach, which surveyed more than 50 chemical species. The analytical protocol is described in [46], whereas the chemical composition, summarizing the major components, is reported in Table 1.

Differential scanning calorimetry (DSC) and thermogravimetric (TG) analyses have been performed in the temperature range 30-500 °C with a scanning rate of 2 °C/min under 50mL/min flux of air using the Mettler Toledo TGA/DSC 3+ instrument.

In situ high-temperature synchrotron powder X-ray diffraction (SR-XRPD) experiments have been carried out at the MCX beamline of the Elettra facility (Trieste, Italy), which experimental setup is described in [53]. The polycrystalline sample of colemanite was loaded in a quartz capillary (300-μm in diameter), which was kept spinning during the data collection. For all the point analyses, a monochromatic incident beam (λ = 0.827 Å) was used and the diffraction patterns were collected using the high-resolution scintillator detector mounted on the four-circle diffractometer available at the beamline. The following data collection strategy was adopted: 2θ range between 5 and 50°, step-width = 0.008°, exposure time 1 s. High-*T* conditions were obtained using a hot gas blower directing a hot air flux on the spinning quartz-capillary, whereas temperature was measured by a thermocouple and previously calibrated using the thermal expansion and phase transition of quartz. A first temperature ramp was performed from ambient conditions (25 °C) up to 375°C, with data collections every 50°C. A second ramp was later performed using the same batch sample at the same experimental conditions of the first ramp from 50 to 250°C, with data collections every 50 °C. Overall, a total of thirteen XRD patterns have been collected at the temperature conditions reported in Table 2.

Full-profile fits were performed by the Rietveld method, using the GSAS [54] and EXPGUI [55] packages. The atomic coordinates reported in [46], for the same colemanite sample, were used as starting model. The background curve was modeled by a Chebyshev polynomial with 19 variable parameters, whereas the peak profiles were modelled using the pseudo-Voigt function of Thomson et al. [56]. The unit-cell and structural parameters of colemanite were also refined adopting the following restraints: 1) displacement parameters were modeled as isotropic (U_{iso}) and the B and O atoms were restrained to share the same U_{iso} group-value, respectively; 2) B^{III}-O and B^{IV}-O (where B^{III} and B^{IV} are boron atoms in triangular and tetrahedral coordination, respectively) bond distances were restrained to 1.36 ± 0.05 and 1.46 ± 0.05 Å, respectively. In addition, the refinement of the fractional occupancy of the H_2O-oxygen atom (Ow) was always tried if the refined value deviated from the full site occupancy (+/- 1σ). In the final cycles of refinement, the following parameters were simultaneously refined: scale factor, background and peak profiles parameters, unit-cell parameters, atomic coordinates and displacement parameters. The zero-shift correction was also refined for the dataset collected at 25 °C and kept constant to this refined value in the Rietveld refinements based on the diffraction patterns collected at higher temperatures. The unit-cell parameters of colemanite at varying temperature are reported in Figure 2 and Table 2. The calculated diffraction patterns, based on the Rietveld refinements at 25 and 225 °C, respectively, are reported in Figure S1 (deposited as supplementary materials). The refined structure models (cif files) are deposited as supplementary materials.

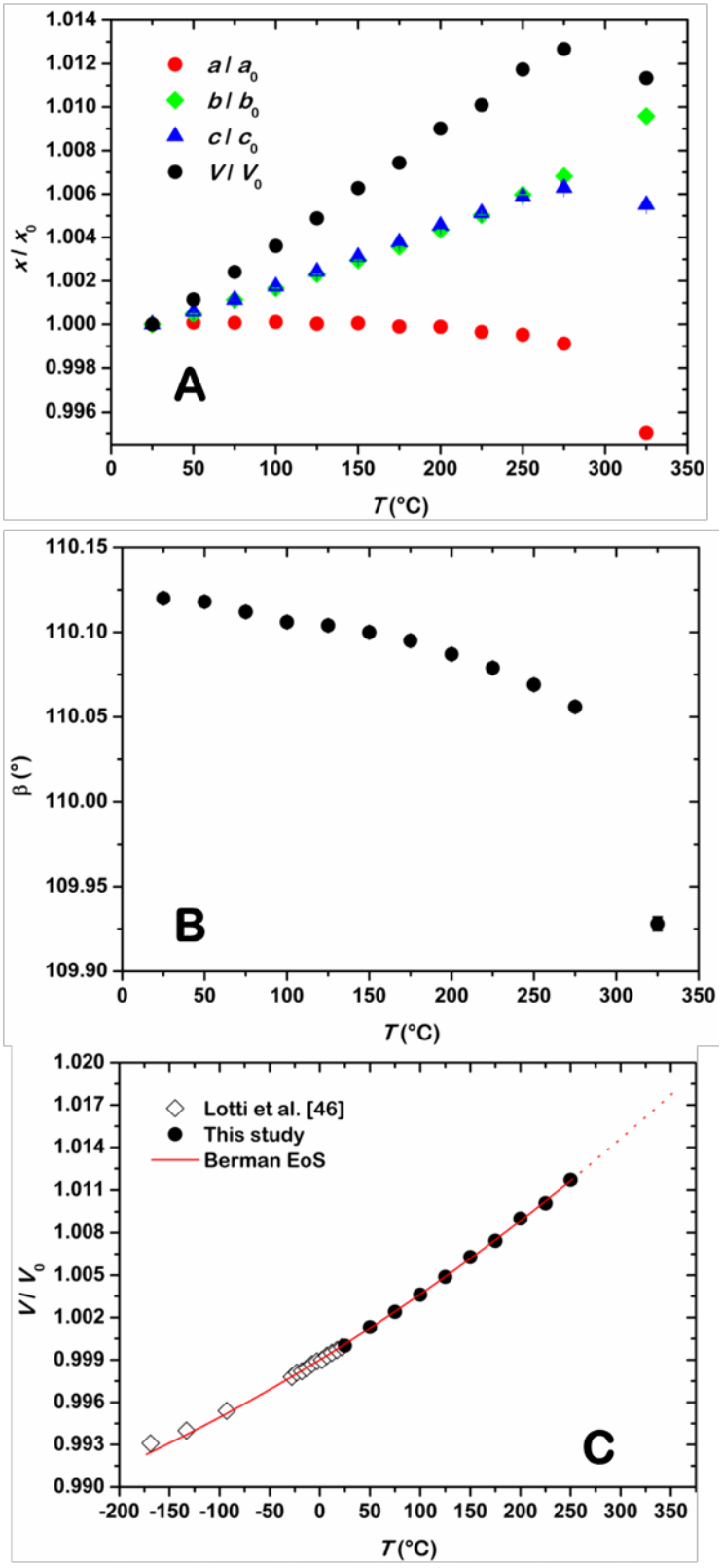

Figure 2. (A). High-temperature evolution of the unit-cell parameters of colemanite, normalized to their ambient-conditions values. (B). High-*T* evolution of the unit-cell monoclinic β angle of colemanite. (C). Unit-cell volume as a function of temperature (normalized to ambient-conditions value) of the same natural sample of colemanite, from this study and from the low-*T* study of Lotti et al. [46]. The refined Berman-type thermal equation of state (EoS) is plotted.

4. Results

4.1. DSC and TG analyses

The differential scanning calorimetry and thermogravimetric data of colemanite are plotted in Figure 3. The main features of the DSC pattern are the following: 1) an endothermic peak at 247°C; 2) a broad exothermic region between 280 and 310°C; 3) two marked endothermic peaks, centered at 372 and 388°C, can be observed, preceded by an inflection point at 345°C and followed by a broad endothermic region up to the highest temperature investigated of 500°C. These endothermic peaks correspond to those already reported in the literature at close temperatures by several authors, e.g. [35,36,38].

The TG pattern shows that the mass loss begins already at $T > 50$°C. Around 240°C, a minor increase in mass loss is observed, whereas at $T > 275$°C a sudden increase in the rate of mass loss occurs. Up to 275°C, the total mass loss is around 1 wt%, whereas it is around 2 wt% at 325°C, where a further increase in the rate of mass loss occurs. At 372 °C (endothermic peak in the DSC plot), the mass loss is 4.05 wt% and at $T > 388$°C (endothermic peak in the DSC plot) a dramatic increase in the mass loss rate is observed with a final weight at 500°C that is 23.03% lower than the initial value.

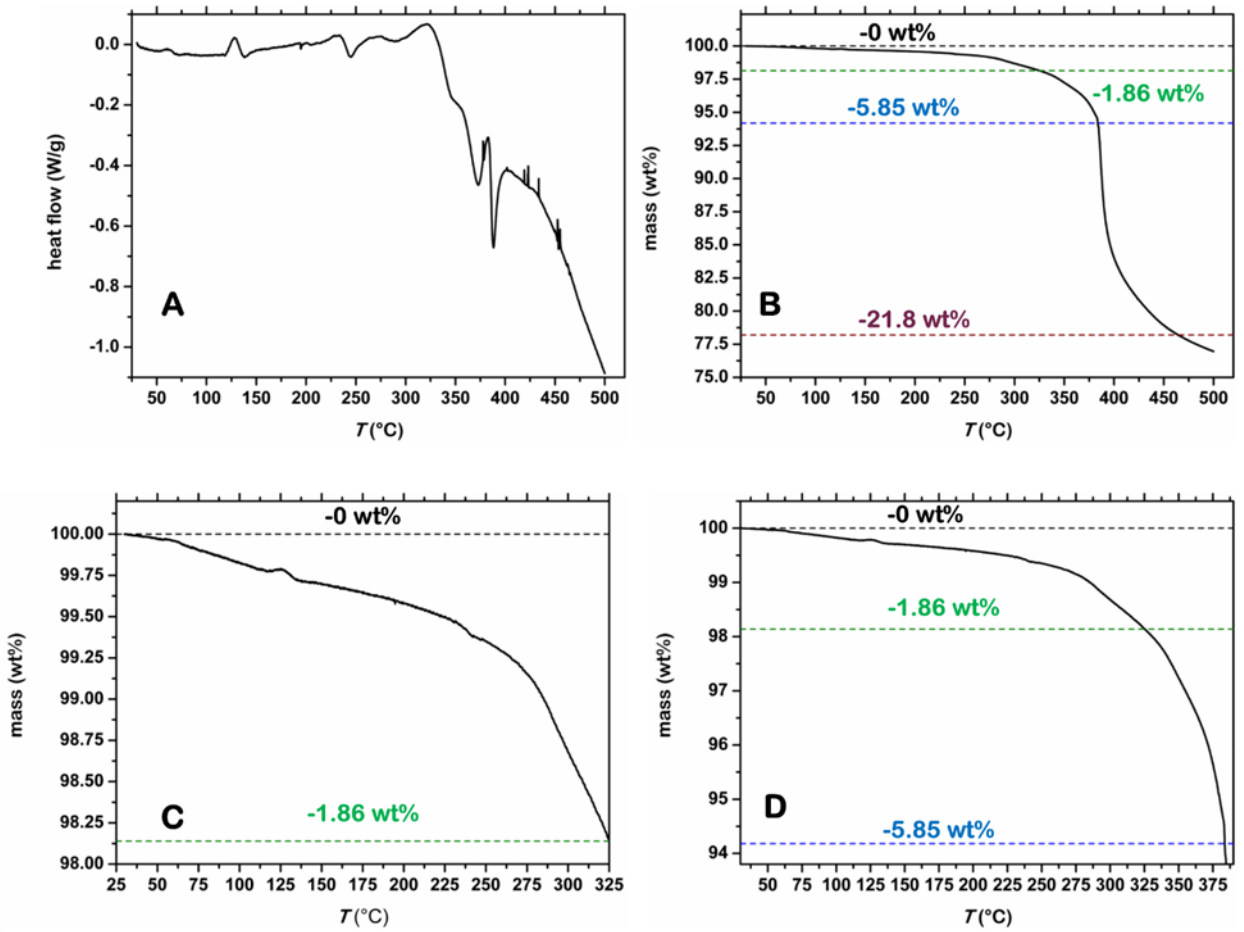

Figure 3. (A). The heat flow rate as a function of temperature, from the full *T*-range investigated by differential scanning calorimetry. (B). The weight loss (in wt%) as a function of temperature, from the full *T*-range investigated by TG analysis. TG data in the *T*-ranges up to 325 and 375 °C are reported in graphs (C) and (D), respectively. For an ease of clarity, the weight losses at -1.86 wt% (corresponding to 325 °C, *i.e.* the highest *T* where crystalline colemanite occurs by XRD data), at -5.85 wt% (corresponding to the contribution of H_2O molecules of colemanite) and at -21.8 wt% (corresponding to the contribution of H_2O molecules and hydroxyl groups) are plotted as reference lines.

4.2. High-temperature behavior of unit-cell parameters and crystal structure

The X-ray diffraction patterns reveal the persistence of a crystalline sample of colemanite up to 325°C (Figure S2, deposited). On the contrary, at 375°C the collected diffraction pattern is typical of an amorphous substance (Figure S3, deposited). The Rietveld refinements reached convergence with good statistical parameters up to 275°C (Table 2), whereas for the pattern collected at 325°C only the unit-cell parameters could be satisfactorily refined.

The refined unit-cell parameters at different temperatures are reported in Table 2 and plotted in Figure 2. The unit-cell *a* edge undergoes a minor expansion up to 175 °C, where a slight contraction rate takes place. At the same temperature, a change in the experimental β-*T* trend can

also be observed. At 275°C, a further deviation from the previous *T*-trends can be observed along the unit-cell **c** axis and for the volume. At 325°C, a significant volume reduction can be observed, governed by the contraction along the **a** and **c** axial edges, whereas the **b** axis shows an opposite behavior with a boosted expansion with respect to the previous *T*-trend.

The refinement of the occupancy of the Ow site was always tried, but the refined value was 1 (within the e.s.d.) up to 250 °C. At 275°C, the Ow refined occupancy was found, for the first time, lower than 1 ($sof = 0.96 \pm 0.02$). Despite the Rietveld refinement of the structural parameters did not converge at 325°C, at least a qualitative analysis of the refined model can be attempted: at this temperature, the site occupancy factor of Ow was ~ 0.77.

The amorphization observed at $T > 325$ °C was found to be irreversible when ambient conditions were recovered.

5. Discussion

5.1. Dehydration mechanism of colemanite

Despite the dehydration mechanism of colemanite has already been investigated by several authors, a clear picture was still not available: Hartung and Heide [35] reported TG and DTA patterns, describing two endothermic peaks coupled with amorphization at ~ 400°C, two exothermic peaks coupled with recrystallization at ~ 800°C and an endothermic peak coupled with melting at ~ 1000°C. Waclawska et al. [36] also reported TG, DTG and DTA data of colemanite, and described the occurrence of two endothermic peaks at 369 and 386°C, respectively. Based on IR spectra, they assigned the first peak to the loss of hydroxyl groups, which would be kept as "*intracrystalline water*" up to the *T* of the second peak, assigned to the explosive release of water and amorphization. Frost et al. [37], based on TG and IR data, reported that the dehydration occurs in a single step at 400.8 °C. Very recently, Rusen [38] reported the first *in situ* high-temperature X-ray diffraction experiment on a commercial sample of colemanite, with minor fractions of quartz and calcite, coupled with TG and DTA analyses. The occurrence of two endothermic peaks at 384 and 399°C, associated to the dehydration of colemanite between 350 and 650°C (and a consequent amorphization) was reported. At 754°C, Rusen [38] reports the crystallization of CaB_2O_4 and $Ca_2B_2O_5$.

A comparative analysis of the DSC and TG patterns of this study, coupled with the Rietveld refinements based on the collected XRD data, allows a thorough description of the dehydration mechanism of colemanite. The TG data show that the dehydration already begins at $T \geq 50$°C (Figure 3). The endothermic peak at 247°C can be coupled with the corresponding minor increase in the rate of mass loss and with the deviations in the *a*-*T* and β-*T* trends observed at $T \geq$ 175°C (Figures 2 and 3, Table 2). At 275°C, the mass loss is around 1 wt% and, for the first time, the refined occupancy of the H_2O-oxygen Ow site is lower than 1.0. Therefore, if up to ~ 240°C the mass loss may also be attributed to moisture or superficial water, the results from DSC, TG and XRD suggest that above this temperature the loss of structural H_2O

unambiguously occurs. At $T > 275$°C, an increase in the rate of mass loss is observed (Figure 3) and at 325°C the dehydration clearly affects the unit-cell volume of colemanite, which undergoes a significant contraction governed by the shortening along the **a** and **c** axes, whereas an expansion along **b** is observed (Figure 2 and Table 2). Despite still crystalline, the structural parameters could not be satisfactorily refined at this temperature, suggesting that the mechanism of structural collapse is triggered and is likely acting along the preferential cleavage plane, *i.e.* (010), where the weaker interactions occur between the adjacent layers made by Ca-polyhedra and borate chains (Figure 1). If we consider, from the chemical composition of colemanite (Table 1), that the total H_2O content is 21.8(4) wt% (of which 15.98 wt% can be attributed to the hydroxyls groups and 5.85 wt% to the H_2O molecules), and that at 325°C the mass loss measured from the TG data is 1.86 wt% (Figure 3), we can conclude that the structural collapse of colemanite is induced in the very early stages of dehydration. Between 325 and 375°C, the amorphization process is completed and a mass loss of 5.85 wt% (corresponding to the weight fraction of structural H_2O molecules) is reached at ~ 382°C (Figure 3), whereas at $T > 388$°C (endothermic peak in the DSC pattern, Figure 3) a significant weight loss is shown by the TG data (Figure 3).

The colemanite dehydration pattern can, therefore, be summarized as in the following:

- At $T > 240$°C, the weight loss is unambiguously attributed to the release of structural H_2O, which is more pronounced at $T \geq 275$°C, triggering the structural collapse that is completed before the H_2O molecules are fully released at $T \sim 375$-385°C;

- The endothermic peak at 388°C may be assigned to the dehydroxylation process;

- At 500°C, the mass loss is 23.03 wt% (Figure 3), that is quite close to the total measured H_2O content of colemanite (i.e., 21.8 wt%), from which it can be concluded that the high-temperature amorphous phase is fully anhydrous, being consistent with the recrystallization of anhydrous Ca-borates reported in [38].

5.2. Thermo-elastic behavior of colemanite

The intrinsic anisotropy and bulk thermal expansion of the compounds used as aggregates concur in controlling the high-temperature behavior of a concrete. For this reason, one of the scope of this work was to characterize the thermo-elastic behavior of colemanite, by determining the bulk thermal expansion coefficient at ambient conditions and as a function of temperature.

The *T*-induced evolution of the unit-cell parameters, reported in Figure 2 and Table 2, reveals that the thermal expansion of colemanite is significantly anisotropic, being substantially accommodated only along the **b** and **c** crystallographic axes, whereas the **a** axis, which corresponds to the direction of the borate chains (Figure 1), experiences only a minor expansion up to 175°C, where a slight contraction takes place (Figure 2 and Table 2). These results are consistent with those reported in [46] for the range 104-300 K (*i.e.*, from -169 to 27 °C) and an analogy can also be found with the high-pressure data [45], where the **a** direction is reported to be the less compressible crystallographic axis.

We merged in a single dataset the unit-cell volume data of this study (excluding the points at 275 and 325°C) and those reported in [46] for the same sample in the range $-169 \leq T\ (°C) \leq 27$, normalizing the data to the respective ambient-T values. The experimental (V/V_0) vs. T data (Figure 2) have been fitted by a Berman T-V equation of state [57] using the EOSFIT7-GUI software [58], yielding the following refined parameters: $V_{25°C} = 563.93(3)$ Å^3, $a_0 = \alpha_{V25°C} = 4.50(10)\cdot10^{-5}$ K^{-1} and $a_1 = 5.7(8)\cdot10^{-8}$ K^{-2}, where $\alpha_V = 1/V\cdot(\partial V/\partial T)_P$. The Berman equation of state is expressed as:

$$V(T) = V(T_0)\cdot[1 + a_0(T - T_0) + 0.5a_1(T - T_0)^2],$$

and $\alpha_V\ [K^{-1}] \approx a_0 + a_1(T - T_0) = 4.50(10)\cdot10^{-5} + 5.7(8)\cdot10^{-8}[T(°C) - 25]$.

In order to quantify the anisotropy of the bulk thermal expansion of colemanite, the l vs. T datasets of this study ($l = a, b, c$) have been fitted by linear Berman-type thermal equations of state using the EOSFIT7-GUI software [58], excluding the points at 275 and 325 °C as for the volume. The refined linear thermo-elastic parameters are reported in the following: $a_{25°C} = 8.7342(3)$ Å, $a_{0(a)} = \alpha_{a25°C} = 0.28(8)\cdot10^{-5}$ K^{-1} and $a_{1(a)} = -4.4(7)\cdot10^{-8}$ K^{-2}; $b_{25°C} = 11.26318(4)$ Å, $a_{0(b)} = \alpha_{b25°C} = 2.1(2)\cdot10^{-5}$ K^{-1} and $a_{1(b)} = 4(2)\cdot10^{-8}$ K^{-2}; $c_{25°C} = 6.1034(2)$ Å, $a_{0(c)} = \alpha_{c25°C} = 2.30(9)\cdot10^{-5}$ K^{-1} and $a_{1(c)} = 3.2(9)\cdot10^{-8}$ K^{-2}. We can, therefore, conclude that the thermal anisotropy at ambient conditions can be expressed as $\alpha_{a25°C} : \alpha_{b25°C} : \alpha_{c25°C} = 1 : 7.5 : 8.2$.

6. Conclusions

The thermal bulk volume (isotropic or anisotropic) expansion and the dehydration mechanism of a given hydrated compound used as an aggregate are important parameters that allow to understand and forecast the behavior of a concrete under heating or cooling. In this study, by means of in situ DSC, TG and XRD data, we have characterized the dehydration mechanism of colemanite, a hydrous Ca-borate mineral used as an aggregate in radiation-shielding concretes, and determined its bulk thermal expansion coefficient along with its expansion anisotropic scheme.

The TG data show that the dehydration already begins at $T \geq 50$°C, whereas the release of structural H_2O unambiguously occurs at least from ~ 240°C. A minor fraction of released H_2O (~ 2 wt%) is sufficient to trigger the structural collapse, which likely acts along the preferential cleavage plane, *i.e.* (010), with a boosted expansion of the **b** crystallographic axis. At $T > 388$°C all the structural H_2O (*i.e.*, H_2O molecules + OH groups) are released and colemanite is irreversibly converted into an anhydrous amorphous phase.

The experimental findings of this study should be carefully considered for the utilization of colemanite as aggregate (expected to preserve its crystalline form) for concretes, as its T-induced structural transformations may impact on the stability of the manufacts, at least at $T \geq 250$°C. This is certainly compatible with colemanite employment in radiation shields of radiotherapy centers and should not represent an issue for most of actual nuclear reactors. By way of example, the temperature of concrete biological shield of the widely prevalent Light Water Reactors

(LWR) is well below 100°C [59]. In the case of High Temperature Gas Reactors (HTGR), where fuel elements can exceed 1000°C, suitable cooling panels are usually installed on the inner concrete wall, in order to maintain the concrete temperature below 50-65°C [60].

Based on the refined thermo-elastic parameters of this study and on the high-pressure elastic parameters reported in [45] for the same sample, it is possible to define the equation of state of colemanite that, at a first approximation, is valid in the ranges $-169 \leq T\,(^{\circ}C) \leq 250$ and $0.0001 \leq P\,(GPa) \leq 13.59$:

$V(T,P) \approx V(T_0,P_0) + \alpha_{VT0}(T - T_0) - \beta_{VT0}(P - P_0) = 563.93(3) + 4.50(10)\cdot10^{-5}(T - T_0) - 0.0149(9)(P - P_0)$, where $T_0 = 25^{\circ}C$ and $P_0 = 0.0001GPa$.

7. Acknowledgements

Alessandro Guastoni (University of Padua) is thanked for having provided the sample of colemanite. Elettra Sincrotrone Trieste is thanked for the allocation of beamtime and provision of synchrotron facilities (proposal number 20170090). PL, DC and GDG acknowledge the support of the Italian Ministry of Education (MIUR) through the project 'Dipartimenti di Eccellenza 2018-2022'.

Declarations of interest: none

Black and white should be used for any figures in print

8. References

[1] M.R. Palmer, G.H. Swihart, Boron Isotope Geochemistry: An Overview, in, L.M. Anovitz, E.S. Grew (Eds.), Boron: Mineralogy, Petrology, and Geochemistry, Rev. Mineral. 33, Mineralogical Society of America, Chantilly, 1996, pp. 709-744.

[2] R.S. Carter, H. Palevsky, V.W. Myers, D.J. Hughes, Thermal neutron absorption cross sections of boron and gold, Phys. Rev. 96 (1953) 716-721.

[3] H. Rauch, W. Waschkowski, Neutron Scattering Lengths, in, A.J. Dianoux, G. Lander (Eds.), Neutron Data Booklet, first ed., Institut Laue Langevin, Grenoble, 2002, pp. 1-18.

[4] D.D. DiJulio, C.P. Cooper-Jensen, H. Perrey, K. Fissum, E. Rofors, J. Scherzinger, P.M. Bentley, A polyethylene-B_4C based concrete for enhanced neutron shielding at neutron research facilities, Nucl. Instrum. Methods A859 (2017) 41-46.

[5] K. Okuno, M. Kawai, H. Yamada, Development of novel neutron shielding concrete, Nucl. Technol. 168 (2009) 545-552.

[6] A. Christogerou, T. Kavas, Y. Pontikes, S. Koyas, Y. Tabak, G.N. Angelopoulos, Use of boron wastes in the production of heavy clay ceramics, Ceram. Int. 35 (2009) 447-452.

[7] E. Erdogmus, Combined effect of waste colemanite and silica fume on properties of cement mortar, Sci. Eng. Compos. Mater. 21 (2014) 369-375.

[8] M. Uysal, M.M. Al-Mashhadani, Y. Aygörmez, O. Canpolat, Effect of using colemanite waste and silica fume as partial replacement on the performance of metakaolin-based geopolymer mortars, Constr. Build. Mater. 176 (2018) 271-282.

[9] T.W. Davies, S. Çolak, R.M. Hooper, Boric acid production by the calcination and leaching of powdered colemanite, Powder Technol, 65 (1991) 433-440.

[10] Y. Yarar, A. Bayülken, Investigation of neutron shielding efficiency and radioactivity of concrete shields containing colemanite, J. Nucl. Mater. 212-215 (1994) 1720-1723.

[11] M. Kinno, K. Kimura, T. Nakamura, Raw Materials for Low-Activation Concrete Neutron Shields, J. Nucl. Sci. Technol. 39 (2002) 1275-1280.

[12] T. Korkut, A. Űn, F. Demir, A. Karabulut, G. Budak, R. Şahin, M. Oltulu, Neutron dose transmission measurments for several new concrete samples including colemanite, Ann. Nucl. Energy 37 (2010) 996-998.

[13] O. Gencel, W. Brostow, C. Ozel, M. Filiz, An investigation on the concrete properties containing colemanite, Int. J. Phys. Sci. 5 (2010) 216-225.

[14] A. Yadollahi, E. Nazemi, A. Zolfaghari, A.M. Ajorloo, Optimization of thermal neutron shield concrete mixture using artifical neural network, Nucl. Eng. Des. 305 (2016) 146-155.

[15] K. Okuno, H. Matsue, S. Miyata, Y. Kiyanagi, Neutron Activation Property of Colemanite-Peridotite Concrete, Nucl. Sci. Eng. 173 (2013) 139-149.

[16] Y. Yarar, Activation characteristics of concrete shields containing colemanite, J. Nucl. Mater. 233-237 (1996) 1511-1515

[17] F. Demir, G. Budak, R. Sahin, A. Karabulut, M. Oltulu, K. Serifoglu, A. Un, Radiation transmission of heavyweight and normal-weight concretes containing colemanite for 6 MV and 18 MV X-rays using linear accelerator, Ann. Nucl. Energy 37 (2010) 339-344.

[18] E.M. Derun, A.S. Kipcak, Characterization of some boron minerals against neutron shielding and 12 year performance of neutron permeability, J. Radioanal. Nucl. Chem. 292 (2012) 871-878.

[19] B. Oto, A. Gür, M.R. Kaçal, B. Dogan, A. Arasoglu, Photon attenuation properties of some concretes containing barite and colemanite in different rates, Ann. Nucl. Energy 51 (2013) 120-124.

[20] O. Içelli, K.S. Mann, Z. Yalçın, S. Orak, V. Karakaya, Investigation of shielding properties of some boron compounds, Ann. Nucl. Energy 55 (2013) 341-350.

[21] H. Binici, O. Aksogan, A. Hayrullah Sevinc, A. Kucukonder, Mechanical and radioactivity shielding performances of mortars made with colemanite, barite, ground basaltic pumice and ground blast furnace slag, Constr. Build. Mater. 50 (2014) 177-183.

[22] T. Korkut, A. Karabulut, G. Budak, B. Aygun, O. Gencel, A. Hancerliogullari, Investigation of neutron shielding properties depending on number of boron atoms for colemanite, ulexite and tincal ores by experiments and FLUKA Monte Carlo simulations, Appl. Radiat. Isotopes 70 (2012) 341-345.

[23] K. Karimi-Shahri, L. Rafat-Motavalli, H. Miri-Hakimabad, Finding a suitable shield for mixed neutron and photon fields based on an Am-Be source, J. Radioanal. Nucl. Chem. 298 (2013) 33-39.

[24] F. Demir, A. Un, Radiation transmission of colemanite, tincalconite and ulexite for 6 and 18 MV X-rays by using linear accelerator, Appl. Radiat. Isotopes 72 (2013) 1-5.

[25] J. Grandjean, A. Joulia, A. Smith, B. Naït-Ali, N. Tessier-Doyen, T. Garnier, F. Labergri, Determination of boron contained in a cementitous matrix used for the transport or the storage of radioactive waste, Prog. Nucl. Energ. 109 (2018) 38-44.

[26] I. Kula, A. Olgun, Y. Erdogan, V. Sevinc, Effects of colemanite waste, cool bottom ash, and fly ash on the properties of cement, Cement Concrete Res. 31 (2001) 491-494.

[27] Ş Targan, A. Olgun, Y. Erdogan, V. Sevinc, Influence of natural pozzolan, colemanite ore waste, bottom ash, and fly ash on the properties of Portland cement, Cement Concrete Res. 33 (2003) 1175-1182.

[28] O. Gencel, M. Naziroglu, Ö Çelik, K. Yalman, D. Bayram, Selenium and Vitamin E Modulates Radiation-Induced Liver Toxicity in Pregnant and Nonpregnant Rat: Effects of Colemanite and Hematite Shielding, Biol. Trace Elem. Res. 135 (2010) 253-263

[29] E. Erdogmus, Y. Erdoğan, O. Gencel, S. Targan, U. Avciata, Influence of colemanite admixture on Portland cement durability, Adv. Cem. Res. 24 (2012) 155-164.

[30] A.G. Celik, T. Depci, A.M. Kilic, New lightweight colemanite-added perlite brick and comparison of its physicomechanical properties with other commercial lightweight materials, Constr. Build. Mater. 62 (2014) 59-66.

[31] Ö.S. Bideci, The effect of high temperature on lightweight concretes produced with colemanite coated pumice aggregates, Constr. Build. Mater. 113 (2016) 631-640.

[32] N. Yaltay, C.E. Ekinci, T. Çakır, B. Oto, Photon attenuation properties of concrete produced with pumice aggregate and colemanite addition in different rates and the effect of curing age to these properties, Prog. Nucl. Energ. 78 (2015) 25-35.

[33] O. Aksogan, H. Binici, E. Ortlek, Durability of concrete made by partial replacement of fine aggregate by colemanite and barite and cement by ashes of corn stalk, wheat straw and sunflower stalk ashes, Constr. Build. Mater. 106 (2016) 253-263.

[34] M.A. Glinicki, A. Antolik, M. Gawlicki, Evaluation of compatibility of neutron-shielding boron aggregates with Portland cement in mortar, Constr. Build. Mater. 164 (2018) 731-738.

[35] E. Hartung, K. Heide, Investigation of Phase Transitions of Hydrated Borates at Non-isothermal Conditions, Krist. Tech. (1978) K57-K60.

[36] I. Waclawska, L. Stoch, J. Paulik, F. Paulik, Thermal decomposition of colemanite, Thermochim. Acta 126 (1988) 307-318.

[37] R.L. Frost, R. Scholz, X. Ruan, R.M. Fernandes Lima, Thermal analysis and infrared emission spectroscopy of the borate mineral colemanite ($CaB_3O_4(OH_3)\cdot H_2O$), J. Therm. Anal. Calorim. 124 (2016) 131-135.

[38] A. Rusen, Investigation of structural behavior of colemanite depending on temperature, Rev. Rom. Mat. 48 (2018) 245-250.

[39] I. Waclawska, Thermal behaviour of mechanically amorphized colemanite. II. Internal structure reconstitution processes of ground Colemanite, J. Therm. Analysis 48 (1997) 155-161.

[40] G.D. Gatta, N. Rotiroti, M. Fisch, T. Armbruster, Stability at high pressure, elastic behavior and pressure-induced structural evolution of "Al_5BO_9", a mullite-type ceramic material, Phys. Chem. Miner. 37 (2010) 227-236.

[41] G.D. Gatta, P. Vignola, G.J. McIntyre, V. Diella, On the crystal-chemistry of londonite [$(Cs,K,Rb)Al_4Be_5B_{11}O_{28}$]: a single-crystal neutron diffraction study at 300 and 20 K, Am. Mineral. 95 (2010) 1467-1472.

[42] G.D. Gatta, P. Vignola, Y. Lee, Stability of $(Cs,K)Al_4Be_5B_{11}O_{28}$ (londonite) at high pressure and high temperature: a potential neutron absorber material, Phys. Chem. Miner. 38 (2011) 429-434.

[43] G.D. Gatta, P. Lotti, M. Merlini, H-P. Liermann, M. Fisch, High-pressure behavior and phase stability of Al_5BO_9, a mullite-type ceramic material, J. Am. Cer. Soc. 96 (2013) 2583-2592.

[44] G.D. Gatta, P. Lotti, D. Comboni, M. Merlini, P. Vignola, H-P. Liermann, High-pressure behaviour of $(Cs,K)Al_4Be_5B_{11}O_{28}$ (londonite): a single-crystal synchrotron diffraction study up to 26 GPa, J. Am. Cer. Soc. 100 (2017) 4893-4901.

[45] P. Lotti, G.D. Gatta, D. Comboni, G. Guastella, M. Merlini, A. Guastoni, H-P. Liermann, High-pressure behavior and *P*-induced phase transition of $CaB_3O_4(OH)_3{\cdot}H_2O$ (colemanite), J. Am. Cer. Soc. 100 (2017) 2209-2220.

[46] P. Lotti, G.D. Gatta, N. Demitri, G. Guastella, S. Rizzato, M.A. Ortenzi, F. Magrini, D. Comboni, A. Guastoni, M.T. Fernandez-Diaz, Crystal chemistry and temperature behavior of the natural hydrous borate colemanite, a mineral commodity of boron, Phys. Chem. Miner. 45 (2018) 405-422.

[47] C.L. Christ, J.R. Clark, H.T. Evans, The stucture of colemanite, $CaB_3O_4(OH)_3{\cdot}H_2O$, determined by the direct method of Hauptman and Karle, Acta Cryst. 7 (1954) 453-454.

[48] C.L. Christ, J.R. Clark, H.T. Evans, Studies of Borate Minerals (III): The Crystal Structure of Colemanite, $CaB_3O_4(OH)_3{\times}H_2O$*, Acta Cryst., 11 (1958) 761-770.

[49] J.R. Clark, D.E. Appleman, C.L. Christ, Crystal chemistry and structure refinement of five hydrated calcium borates, J. Inorg. Nucl. Chem. 26 (1964) 73-95.

[50] H.H. Wieder, A.R. Clawson, C.R. Parkerson, Ferroelectric and Pyroelectric Properties of Mineral and Synthetic Colemanite, J. Appl. Phys. 33 (1962) 1720-1725.

[51] F.N. Hainsworth, H.E. Petch, The structural basis of ferroelectricity in colemanite, Can. J. Phys. 44 (1966) 3083-3107.

[52] C. Helvaci, Stratigraphy, Mineralogy, and Genesis of the Bigadiç Deposits, Western Turkey, Econ. Geol. 90 (1995) 1237-1260.

[53] L. Rebuffi, J.R. Plaisier, M. Abdellatief, A. Lausi, P. Scardi, MCX: a Synchrotron Radiation Beamline for X-ray Diffraction Line Profile Analysis, Z. Anorg. Allg. Chem. 640 (2014) 3100-3106.

[54] A.C. Larson, R.B. Von Dreele, General Structure Analysis System (GSAS), Los Alamos National Laboratory Report, Los Alamos, 2004.

[55] B.H. Toby, EXPGUI, a graphical user interface for GSAS, J. Appl. Crystallogr. 34 (2001) 210-221.

[56] P. Thompson, D.E. Cox, J.B. Hastings, Rietveld refinement of Debye-Scherrer synchrotron X-ray data from Al_2O_3, J. Appl. Crystallogr. 20 (1988) 79-83.

[57] R.G. Berman, Internally-consistent thermodynamic data for minerals in the system Na_2O–K_2O–CaO–MgO–FeO–Fe_2O_3–Al_2O_3–SiO_2–TiO_2–H_2O–CO_2, J. Petrol. 29 (1988) 445-522.

519 [58] J. Gonzalez-Platas, M. Alvaro, F. Nestola, R.J. Angel, EosFit7-GUI: a new graphical user
520 interface for equation of state calculations, analyses and teaching, J. Appl. Crystallogr. 49 (2016)
521 1377-1382.

522 [59] K.G. Field, I. Remec, Y. Le Pape, Radiation effects in concrete for nuclear power plants -
523 Part I: Quantification of radiation exposure and radiation effects, Nucl. Eng. Des. 282 (2015)
524 126-143.

525 [60] IAEA, TECDOC-1694: Evaluation of high temperature gas cooled reactor performance,
526 Vienna (2013), ISBN 978-92-0-137610-7.

527 [61] K. Momma, F. Izumi, VESTA 3 for three-dimensional visualization of crystal, volumetric
528 and morphology data, J. Appl. Crystallogr. 44 (2011) 1272-1276.

529 [62] J.W. Anthony, R.A. Bideaux, K.W. Bladh, M.C. Nichols (Eds.) Handbook of Mineralogy,
530 Mineralogical Society of America, Chantilly,
531 http://www.handbookofmineralogy.org/pdfs/colemanite.pdf.

532

Figure captions

Figure 1. (*Left*) The crystal structure of colemanite viewed down the **b** crystallographic axis, showing the heteropolyhedral layers made by alternating borate and Ca-polyhedra chains. Every borate chain is made by the repetition of three-membered rings, formed by one boron site in triangular coordination and two boron sites in tetrahedral coordination. (*Right*). The colemanite structure viewed down the **c** axis: the heteropolyhedral layers are weakly interconnected by few Ca-O(H)-B bonds and by a network of H-bonds. These pictures have been created using the software VESTA [61].

Figure 2. (A). High-temperature evolution of the unit-cell parameters of colemanite, normalized to their ambient-conditions values. (B). High-*T* evolution of the unit-cell monoclinic β angle of colemanite. (C). Unit-cell volume as a function of temperature (normalized to ambient-conditions value) of the same natural sample of colemanite, from this study and from the low-*T* study of Lotti et al. [46]. The refined Berman-type thermal equation of state (EoS) is plotted.

Figure 3. (A). The heat flow rate as a function of temperature, from the full *T*-range investigated by differential scanning calorimetry. (B). The weight loss (in wt%) as a function of temperature, from the full *T*-range investigated by TG analysis. TG data in the *T*-ranges up to 325 and 375 °C are reported in graphs (C) and (D), respectively. For an ease of clarity, the weight losses at -1.86 wt% (corresponding to 325 °C, *i.e.* the highest *T* where crystalline colemanite occurs by XRD data), at -5.85 wt% (corresponding to the contribution of H_2O molecules of colemanite) and at -21.8 wt% (corresponding to the contribution of H_2O molecules and hydroxyl groups) are plotted as reference lines.

558

559 **Table 1.** *(Left).* The mass fractions (in oxides wt%) of the main chemical components of the
560 investigated natural sample of colemanite, as obtained by a multi-methodological approach
561 described in [46]. (*Right*). Selected physical properties of colemanite.

	wt%
B_2O_3	50.8(4)
CaO	27.2(2)
SrO	0.30(5)
SiO_2	0.03(1)
H_2O	21.8(4)

Density	[g/cm^3]	2.423(5)	[62]
Hardness	[Mohs scale]	4.5	[62]
α_{V0}	[K^{-1}]	$4.50(10)\cdot10^{-5}$	This study
β_{V0}	[GPa^{-1}]	0.0149(9)	[45]
The low-*T* polymorph of colemanite (space group $P2_1$ [46]) is pyroelectric and piezoelectric [50].			

562

563

Table 2. Unit-cell parameters of colemanite and details pertaining to the structure refinements performed at different temperatures

Ramp 1

T (°C)	25	75	125	175	225	275	325[***]
Space group	$P2_1/a$	$P2_1/a$	$P2_1/a$	$P2_1/a$	$P2_1/a$	$P2_1/a$	$P2_1/a$
a (Å)	8.7342(2)	8.7348(2)	8.7344(2)	8.7333(2)	8.7312(2)	8.7268(2)	8.6863(9)
b (Å)	11.2646(2)	11.2774(2)	11.2906(2)	11.3049(2)	11.3212(2)	11.3413(2)	11.3745(8)
c (Å)	6.10352(9)	6.11049(8)	6.11840(8)	6.12661(8)	6.1348(1)	6.1418(2)	6.1348(6)
β (°)	110.120(1)	110.112(1)	110.104(1)	110.095(1)	110.080(1)	110.056(2)	109.913(8)
V (Å^3)	563.86(1)	565.219(8)	566.612(8)	568.053(8)	569.547(9)	571.01(2)	569.89(6)
Observed peaks [$F_o^2/\sigma(F_o^2)>3$]	662	662	663	666	667	670	686
Refined param.	67[*]	66	66	66	66	67[**]	67[**]
$R(F^2)$ (obs)	0.0848	0.0907	0.0921	0.1035	0.1157	0.1675	0.1415
R_{peaks} (fitted)	0.0885	0.0897	0.0903	0.0925	0.0993	0.1167	0.1279
wR_{peaks} (fitted)	0.1118	0.1137	0.1143	0.1178	0.1264	0.1522	0.1737
Residuals (e^-/Å^3)	+0.94 -0.56	+1.03 -0.60	+1.00 -0.54	+1.22 -0.62	+1.32 -0.69	+1.66 -0.95	+2.09 -0.73
s.o.f. (Ow)	1.0	1.0	1.0	1.0	1.0	0.96(2)	0.77(3)

Ramp 2

T (°C)	50	100	150	200	250
Space group	$P2_1/a$	$P2_1/a$	$P2_1/a$	$P2_1/a$	$P2_1/a$
a (Å)	8.7349(2)	8.7351(2)	8.7346(2)	8.7332(2)	8.7301(2)
b (Å)	11.2699(2)	11.2834(2)	11.2979(2)	11.3135(2)	11.3318(2)
c (Å)	6.10707(9)	6.11423(8)	6.12257(8)	6.13128(9)	6.1394(2)
β (°)	110.118(1)	110.109(1)	110.100(1)	110.088(1)	110.069(2)
V (Å^3)	564.509(9)	565.895(8)	567.396(9)	568.939(9)	570.47(1)

Observed peaks [$F_o^2/\sigma(F_o^2)>3$]	662	660	660	667	669
Refined param.	66	66	66	66	66
$R(F^2)$ (obs)	0.1301	0.1047	0.1246	0.1386	0.1524
R_{peaks} (fitted)	0.1037	0.0978	0.1023	0.1041	0.1130
wR_{peaks} (fitted)	0.1468	0.1255	0.1302	0.1325	0.1442
Residuals	+1.66	+1.62	+1.64	+1.64	+1.95
(e^-/Å^3; fm/Å^3)	-0.97	-0.62	-0.63	-0.78	-0.99
s.o.f. (Ow)	1.0	1.0	1.0	1.0	1.0

* Zero shift refined. The value refined for the 25°C data has been kept constant during the Rietveld refinements based on the experimental data collected at higher temperatures.

** Ow site occupancy factor refined

*** Rietveld refinement at 325°C did not reach convergence